*J Mater Sci* (2024) 59:17079–17095

Computation & theory

# Design and characterization of structural, mechanical, electronic, and optical properties of $Cr_xMo_{1-x}S_2$ alloys for advanced material applications

Behdad Moslehi[1], Zahra Nourbakhsh[1,*], and Daryoosh Vashaee[2,3,*]

[1] Faculty of Physics, University of Isfahan, Isfahan, Iran
[2] Department of Electrical and Computer Engineering, North Carolina State University, Raleigh, USA
[3] Department of Materials Science and Engineering, North Carolina State University, Raleigh, USA

**Received:** 9 March 2024
**Accepted:** 5 September 2024
**Published online:** 19 September 2024



## ABSTRACT

This study presents a comprehensive analysis of the electronic, mechanical, and optical properties of $Cr_xMo_{1-x}S_2$, a bulk transition metal dichalcogenide. Using density functional theory with spin–orbit interaction, we employed both the generalized gradient approximation (GGA) and the modified Becke–Johnson potential (mBJ-GGA) to evaluate these properties. Our results confirm that all $Cr_xMo_{1-x}S_2$ alloys are nonmagnetic and thermodynamically stable, as evidenced by cohesive energy calculations. Mechanical assessments comply with Born's criteria, further affirming their stability. Interestingly, lower concentrations of Cr, particularly in $Cr_{0.125}Mo_{0.875}S_2$, significantly enhance atomic bond strength and elastic stiffness. Additional mechanical analysis, including the universal elastic anisotropy index, microhardness, machinability index, and Pugh's criterion, reveals that all alloys are anisotropic and brittle, with $Cr_{0.375}Mo_{0.625}S_2$ and $Cr_{0.625}Mo_{0.375}S_2$ demonstrating superior machinability. On the electronic front, the addition of Cr substantially modifies the $MoS_2$ bandgap and the density of states near the Fermi level. Even at low Cr concentrations, a significant reduction in the energy bandgap is observed, with notable contributions from Cr-$d_{z^2}$ orbitals to the valence and conduction bands. Optically, we examined the dielectric constant $\varepsilon(\omega)$ components, along with absorption ($\alpha(\omega)$), reflection ($R(\omega)$), and refraction ($n(\omega)$) coefficients in both X and Z directions. An increase in Cr concentration leads to a redshift in these properties, with prominent peaks in the visible light spectrum, especially in the yellow and blue light energies. The thorough examination of electronic, mechanical, and optical properties suggests that $Cr_xMo_{1-x}S_2$ alloys hold significant potential for various applications in electronic and optical technologies, particularly in areas requiring bandgap engineering.

Handling Editor: Scott Beckman.

Address correspondence to E-mail: z.nourbakhsh@sci.ui.ac.ir; dvashae@ncsu.edu

https://doi.org/10.1007/s10853-024-10197-3

## Introduction

Historically, alloying has been an effective technique for modifying the electronic structure of semiconductor materials, as extensively documented in the literature [1–3]. An alloy is essentially a mixture or solution comprising two or more elements, which often exhibits unique characteristics distinct from those of its individual components. The interactions within an alloy can vary, ranging from covalent to electrostatic interactions in ionic bonds. For instance, $MoS_2$ is a compound where Mo atoms are bonded to S atoms, but $Cr_xMo_{1-x}S_2$ is an alloy comprising both $CrS_2$ and $MoS_2$ in a specified x:(1-x) molar ratio [4]. Through varying the molar ratios in such alloys, it is possible to engineer changes in the energy bandgap and lattice parameters, thereby enhancing their photoelectric and catalytic performance [5].

In recent years, transition metal dichalcogenides (TMDs) have received considerable attention owing to their unique characteristics, which include high mechanical strength, a direct bandgap, and optical transparency [6–9]. Despite this, the field of alloying these materials still demands more exploration [4, 5]. TMDs follow a general $AB_2$ formula, where A is a transition metal (like Mo, W, Cr, etc.) and B is a chalcogen (such as S, Se, and Te). These compounds can exist in more than 40 different forms, with their electronic structures ranging from metallic (e.g., $VS_2$, $NbS_2$) to semiconductor (e.g., $WS_2$, $MoS_2$) [10–13]. In terms of crystal structure, TMDs are divided into two most stable groups: the honeycomb (2H) with D6h symmetry and centered honeycomb (1T) with D3d symmetry. Both these crystal structures comprise three layers of atoms, where a layer of A atoms is sandwiched between two layers of B atoms. The atoms in these structures are held together by weak out-of-plane van der Waals interactions (between the layers) and strong in-plane chemical interactions (within the layers) [14].

The unique structural features of TMDs have led to their widespread use in both fundamental and applied research. As a significant member of the 2D material family, TMDs, particularly $MoS_2$, exhibit promising applications across various electronic and energy-related fields. These materials are utilized as electrodes in lithium-ion batteries [15], where their high surface area and excellent conductivity enhance energy storage capabilities. Additionally, TMDs are integral components in rechargeable batteries [16], offering improved charge–discharge cycles and stability.

In the realm of renewable energy, TMDs serve as efficient materials for solar cells [17], owing to their tunable bandgaps and high absorption coefficients. Their sensitivity to environmental changes makes them suitable for gas sensors [18], where they detect trace amounts of gases with high precision. Moreover, TMDs play a crucial role in the hydrogen evolution reaction (HER) [19, 20], acting as effective catalysts due to their active edge sites and catalytic properties.

TMDs are also prominent in electrocatalysis [21–23], where their unique electronic structures facilitate various electrochemical reactions. In optoelectronic applications, TMDs, including $MoS_2$, form heterostructures that enable novel functionalities in devices such as photodetectors and light-emitting diodes. These materials are pivotal in the development of electronic devices like field-effect transistors (FETs) [24, 25], where their high on–off ratios and carrier mobility contribute to enhanced device performance.

Recent advancements have also highlighted the potential of TMDs in plasmonic applications, where their interaction with light at the nanoscale enables significant enhancements in optical properties. Studies have demonstrated the utility of TMD-based heterostructures in optoelectronic devices, leveraging their plasmonic properties to improve efficiency and functionality [23, 26, 27].

Among the various TMDs, $MoS_2$ has been of particular interest due to its unique semiconducting properties, which are similar to those of carbon-based graphite [28, 29]. Research on $MoS_2$ has predominantly focused on fabrication techniques [30], bandgap engineering [31, 32], and the development of 2D $MoS_2$ for electrocatalytic applications by structural engineering [26, 27, 33]. Given the similarity in the structures of TMDs, $MoS_2$ can readily form alloys with other TMDs. Furthermore, the versatility of TMDs provides a new route to achieve suitable electronic structures by creating complex alloys. In the alloying process of TMDs, if the two components share a structural phase, they may form homogeneous alloys (solid solutions), with both types of metals occupying positions in the system. However, if solid solutions are thermodynamically unstable, they tend to form heterostructures [34–36]. In essence, the atomic structure has a profound impact on the electronic structure of TMDs. Therefore, understanding the intricate details of the

structural phase and electronic properties is vital for the design of TMD alloys.

In this study, following an investigation of structural stability, $MoS_2$, which is stable in the 2H structural phase (2H-$MoS_2$), was selected. Due to the stability of $CrS_2$ in the 2H structural phase, the Cr atom was chosen to create the $Cr_xMo_{1-x}S_2$ alloy. To form the $Cr_xMo_{1-x}S_2$ alloy with compositions x = 0, 0.125, 0.25, 0.375, 0.50, 0.625, 0.75, 0.875, and 1, a 2 × 2 × 1 supercell of 2H-$MoS_2$ was utilized, and some Mo atoms were replaced with Cr atoms. Following optimization, the structural, mechanical, electronic, and optical properties of this alloy were thoroughly investigated.

## Method

In this research, the WIEN2k computational package, based on density functional theory (DFT), was utilized for all calculations [37]. This package allows for detailed investigation of materials' properties at the atomic level. For the exchange–correlation potential, two approaches were employed: the generalized gradient approximation (GGA) and the generalized gradient approximation augmented with the modified Becke–Johnson potential (mBJ-GGA). These methods are well-established in the field for analyzing the electronic properties of materials.

The $R_{mt}K_{max}$ parameter, crucial in DFT calculations, was set at 8. This parameter represents a balance between computational efficiency and accuracy, with $R_{mt}$ denoting the smallest radius of the unit cell atomic sphere and $K_{max}$ being the largest reciprocal lattice vector [38–40]. The separation energy between core and conduction electrons was chosen as -6 Ry, a standard value in such computational studies.

Our study focused on varying concentrations of Cr within the $MoS_2$ crystal to form $Cr_xMo_{1-x}S_2$. The structural, mechanical, electronic, and optical properties of these alloys were systematically investigated under these varying concentrations. The Brillouin zone (BZ) of $Cr_xMo_{1-x}S_2$ was sampled using 9 × 9 × 4 k-meshes for structural and electronic calculations, which provides a reliable resolution for these types of calculations.

For optical calculations, a finer k-mesh of 17 × 17 × 6 was used to sample the BZ. This higher resolution mesh was selected to ensure a more detailed analysis of the optical properties, which can be sensitive to subtle changes in the material's structure and composition.

## Results and discussion

### Structural and mechanical properties

Transition metal dichalcogenides (TMDs), such as $MoS_2$ and $CrS_2$, exhibit various polymorphs including hexagonal, tetragonal, and monoclinic structures [41]. Hexagonal structures, in which the transition metal layer (Mo or Cr) is sandwiched between two sulfur (S) layers through covalent bonds, have been identified as semiconductors and are the most stable configurations [42–44]. In line with these findings, we selected the hexagonal structure of $MoS_2$ for our study due to its semiconductor nature, stability, and nonmagnetic properties. Figure 1a shows the top and side views of the hexagonal $MoS_2$ TMD.

To synthesize $Cr_xMo_{1-x}S_2$ alloys with varying Cr concentrations, a 2 × 2 × 1 supercell of $MoS_2$ was constructed. This supercell contains 8 Mo atoms, and to create the alloys, Cr atoms were substituted at different ratios x = m/8 (where m ranges from 1 to 8). The resulting structures, depicted in Fig. 1(b 1–7), include seven alloys: $Cr_{0.125}Mo_{0.875}S_2$, $Cr_{0.250}Mo_{0.750}S_2$, $Cr_{0.375}Mo_{0.625}S_2$, $Cr_{0.500}Mo_{0.500}S_2$, $Cr_{0.625}Mo_{0.375}S_2$, $Cr_{0.750}Mo_{0.250}S_2$, and $Cr_{0.875}Mo_{0.125}S_2$. These alloys predominantly exhibit a monoclinic structure with a 6-Pm space group, except for $MoS_2$ and $CrS_2$, which have hexagonal structures with P63/mmc space group.

Our investigation into the magnetic properties of $Cr_xMo_{1-x}S_2$ alloys, as detailed in the supplementary file, reveals a significant finding. The total crystal energy changes, both with and without spin-polarization (SP) calculations, were analyzed as a function of crystal volume. The results are graphically represented in Fig. S1 in the supplementary file, and suggest that the presence of SP does not significantly lower the crystal energy. This implies that these alloys are nonmagnetic, a conclusion that aligns with previous studies. Consequently, we ignore the SP in our calculations. For a more comprehensive understanding of the methods and results, we refer readers to the supplementary file accompanying this manuscript.

Post-optimization, the lattice parameters of the $Cr_xMo_{1-x}S_2$ alloys were calculated using the GGA approach and are presented in Table 1. The lattice

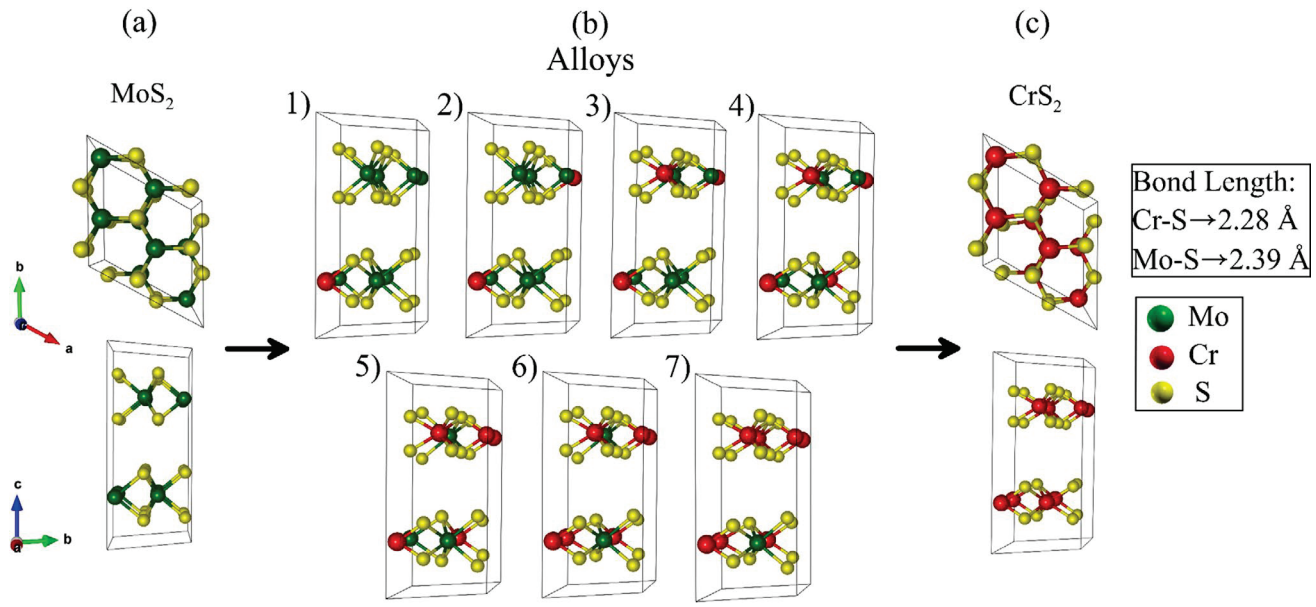


**Figure 1** **a** Top and side views of the $MoS_2$ structure, illustrating its layered configuration. **b** Side views of the $Cr_xMo_{1-x}S_2$ alloys with a range of Cr concentrations. The images depict: 1) $Cr_{0.125}Mo_{0.875}S_2$ 2) $Cr_{0.250}Mo_{0.750}S_2$ 3) $Cr_{0.375}Mo_{0.625}S_2$ 4) $Cr_{0.500}Mo_{0.500}S_2$ 5) $Cr_{0.625}Mo_{0.375}S_2$ 6) $Cr_{0.750}Mo_{0.250}S_2$ and 7) $Cr_{0.875}Mo_{0.125}S_2$ alloys. **c** Top and side views of the $CrS_2$ structure. Mo atoms are represented by green spheres, Cr atoms by red spheres, and S atoms by yellow spheres. The unit cells are delineated with fine lines for clear demarcation.

parameters obtained for $MoS_2$ and $CrS_2$ align well with those reported in previous studies. It is noteworthy that this research represents the first investigation of the structural features of the $Cr_xMo_{1-x}S_2$ alloy in its bulk form, hence no prior data on its lattice parameters or other structural characteristics are available for comparison.

To evaluate the potential for experimental synthesis of $Cr_xMo_{1-x}S_2$ alloy, the cohesive energy was calculated. Cohesive energy, defined as the energy required to disassemble a compound into its constituent atoms [45, 46], was determined using the equation:

$$E_c = \left(E_{tot} - N_{Cr}E_{Cr} - N_{Mo}E_{Mo} - N_S E_S\right)/N_{tot} \quad (1)$$

Here, $E_{tot}$, $E_{Cr}$, $E_{Mo}$, and $E_S$ represent the total energy of the alloy and the isolated energies of Cr, Mo, and S atoms, respectively. $N_{tot}$, $N_{Cr}$, $N_{Mo}$, and $N_S$ denote the number of total, Cr, Mo, and S atoms in the unit

**Table 1** Comparative analysis of theoretical and experimental lattice parameters, crystalline volume, and cohesive energy for pristine $MoS_2$, $CrS_2$, and $Cr_xMo_{1-x}S_2$ alloys across various chromium concentrations

| Structure | Method | a (Å) | c (Å) | Others report | Cohesive energy (eV/atom) |
|---|---|---|---|---|---|
| $MoS_2$ | GGA | 6.24 | 13.31 | 6.36[a], 12.27[a] 6.32[b], 12.29[b] | −7.25 |
| $Cr_{0.125}Mo_{0.875}S_2$ | GGA | 6.22 | 13.37 | | −7.10 |
| $Cr_{0.250}Mo_{0.750}S_2$ | GGA | 6.29 | 13.13 | | −7.06 |
| $Cr_{0.375}Mo_{0.625}S_2$ | GGA | 6.27 | 13.21 | | −6.95 |
| $Cr_{0.500}Mo_{0.500}S_2$ | GGA | 6.26 | 13.25 | | −6.85 |
| $Cr_{0.625}Mo_{0.375}S_2$ | GGA | 6.19 | 13.34 | | −6.74 |
| $Cr_{0.750}Mo_{0.250}S_2$ | GGA | 6.15 | 13.41 | | −6.63 |
| $Cr_{0.875}Mo_{0.125}S_2$ | GGA | 6.13 | 13.09 | | −6.51 |
| $CrS_2$ | GGA | 6.24 | 13.20 | 6.04[c], 12.15[c] | −6.40 |

[a]Ref. [80], [b]Ref. [81], [c]Ref [82]

cell of the alloy [47, 48]. The calculated cohesive energies are presented in Table 1. The negative values of cohesive energies indicate the experimental synthesizability of these alloys. Notably, an increase in Cr concentration corresponds to a decrease in cohesive energy, suggesting that alloys with lower Cr concentrations are more energetically stable than those with higher concentrations.

Elastic properties are crucial in understanding several aspects of crystalline structures, such as structural stability, hardness, and ductility or brittleness. Elastic constants and moduli are particularly informative about a crystal's behavior under stress [49]. Generally, the elastic tensor $C_{ij}$ has 21 components, which are reduced by the presence of symmetry [50]. In this study, the alloys exhibited two structural phases: hexagonal ($MoS_2$, $CrS_2$, and $Cr_{0.500}Mo_{0.500}S_2$) and monoclinic (other alloys). To explore the correlation between Cr concentration and mechanical response, we investigated their elastic properties using the IR-elast + wien2k computing package with the GGA approach. The results are detailed in Table 2. The hexagonal space group alloys have five independent elastic constants $C_{11}$, $C_{12}$, $C_{13}$, $C_{33}$ and $C_{44}$, with others like $C_{66} = (C_{11} - C_{12})/2$ being dependent [51]. The elastic constants obtained for $MoS_2$ and $CrS_2$ closely align with previously reported values [52–55]. However, to our knowledge, there is no available data for direct comparison with the elastic constants of these alloys.

Furthermore, to assess the mechanical stability of $Cr_xMo_{1-x}S_2$ alloys, we applied the Born mechanical stability criteria [56]. These criteria are sets of inequalities for the elastic constants, derived from the requirement for positive elastic properties, and are as follows:

$$C_{11} > 0, C_{33} > 0, C_{44} > 0 \tag{2}$$

$$(C_{11} - C_{12}) > 0 \tag{3}$$

$$(C_{11} + C_{12}) > C_{33} - 2C_{13}^2 > 0 \tag{4}$$

As per Table 2, the elastic constants for all Cr concentrations are positive, confirming that all the investigated alloys satisfy the Born criteria and are mechanically stable at zero pressure.

To further elucidate the mechanical properties of $Cr_xMo_{1-x}S_2$ alloys, the bulk modulus (B), shear modulus (G), and Young's modulus (Y) were calculated using Voigt, Reuss, and Hill approximations. The Voigt and Reuss approximations differ in their consideration of strain and stress: the Voigt approximation assumes uniform strain ratios throughout the crystal, whereas the Reuss approximation assumes uniform stress ratios [57, 58]. For hexagonal structures, the bulk and shear moduli with Voigt ($B_v$ and $G_v$) and Reuss ($B_R$ and $G_R$) approximations are computed using the following equations [52]:

$$B_v = \frac{2(C_{11} + C_{12}) + 4C_{13} - C_{33}}{2} \tag{5}$$

**Table 2** Elastic constants ($C_{ij}$) in GPa for $Cr_xMo_{1-x}S_2$ alloys: a comparative study with previous calculations

| | $C_{11}$ | $C_{22}$ | $C_{33}$ | $C_{44}$ | $C_{55}$ | $C_{66}$ | $C_{12}$ | $C_{13}$ | $C_{23}$ | $C_{15}$ | $C_{25}$ | $C_{35}$ | $C_{46}$ |
|---|---|---|---|---|---|---|---|---|---|---|---|---|---|
| $MoS_2$ | 194.1 | 194.1 | 11.4 | 3.7 | 3.7 | 72.3 | 49.3 | 2.9 | 2.9 | | | | |
| | 191[a] | 191[a] | 15[a] | 7[a] | 7[a] | 72[a] | 46[a] | −5[a] | −5[a] | | | | |
| | 211[b] | 211[b] | 37[b] | 30[b] | 30[b] | 81[b] | 49[b] | 3[b] | 3[b] | | | | |
| $Cr_{0.125}Mo_{0.875}S_2$ | 199.3 | 19.4 | 203.1 | 4.8 | 74.0 | 4.7 | 3.4 | 49.1 | 4.4 | −0.02 | 0.04 | −0.02 | 0.18 |
| $Cr_{0.250}Mo_{0.750}S_2$ | 197.6 | 18.2 | 207.4 | 4.2 | 72.9 | 4.2 | 4.6 | 48.2 | 4.2 | −0.04 | 0.05 | −0.02 | 0.17 |
| $Cr_{0.375}Mo_{0.625}S_2$ | 181.4 | 4.6 | 177.7 | 0.7 | 67 | 0.9 | 0.7 | 47.1 | 1.2 | −1.2 | 0.05 | −0.06 | −0.14 |
| $Cr_{0.500}Mo_{0.500}S_2$ | 176.5 | 5.4 | 179.9 | 1.3 | 63.6 | 1.1 | 1.3 | 45.8 | 1.2 | −1.3 | −0.05 | −0.2 | −0.11 |
| $Cr_{0.625}Mo_{0.375}S_2$ | 180.1 | 4.5 | 177 | 0.5 | 66.8 | 0.9 | 0.6 | 46.8 | 0.8 | −1.3 | −0.1 | −0.4 | −0.1 |
| $Cr_{0.750}Mo_{0.250}S_2$ | 207.8 | 11.8 | 211.2 | 3.09 | 78.4 | 3 | 2.9 | 48.7 | 2.9 | 0.2 | −0.1 | −0.01 | −0.1 |
| $Cr_{0.875}Mo_{0.125}S_2$ | 209.1 | 13.1 | 205.5 | 4.2 | 79.8 | 3.5 | 1.6 | 49.5 | 2.1 | −0.04 | −0.05 | −0.02 | −0.01 |
| $CrS_2$ | 121.07 | 121.07 | 17.7 | 7.7 | 7.7 | 41.2 | 38.6 | 6.06 | 6.06 | | | | |
| | 120[c] | 120[c] | | | | 44[c] | 31[c] | | | | | | |

[a]Ref. [52], [b]Ref. [54], [c]Ref. [55]

$$B_R = \frac{(C_{11}+C_{13})C_{33} - 2C_{13}^2}{C_{11}+C_{12}+2C_{33}+4C_{13}} \quad (6)$$

$$G_v = \frac{(C_{11}+C_{12}) - 2C_{33} + 4C_{13} + 12C_{44} + 12C_{66}}{30} \quad (7)$$

$$G_R = \frac{(C_{11}+C_{13})C_{33} - 2C_{13}^2}{2\left(3B_vC_{44}C_{66} + \left((C_{11}+C_{12})C_{33} + 2C_{13}^2\right)(C_{44}+C_{66})\right)} \quad (8)$$

In monoclinic structures, the bulk and shear moduli are calculated as follows [57]:

$$B_v = \frac{1}{9}(C_{11}+C_{22}+C_{33}) + \frac{2}{9}(C_{12}+C_{23}+C_{13}) \quad (9)$$

$$G_v = \frac{1}{15}(C_{11}+C_{22}+C_{33}) - \frac{1}{15}(C_{12}+C_{23}+C_{13}) + \frac{1}{5}(C_{44}+C_{55}+C_{66}) \quad (10)$$

$$\frac{1}{B_R} = (S_{11}+S_{22}+S_{33}) + 2(S_{12}+S_{23}+S_{13}) \quad (11)$$

$$\frac{1}{G_R} = \frac{4}{15}(S_{11}+S_{22}+S_{33}) - \frac{4}{15}(S_{12}+S_{23}+S_{13}) + \frac{1}{5}(S_{44}+S_{55}+S_{66}) \quad (12)$$

Here, $S_{ij}$ represent the elastic compliance constants. The Hill approximation [59], which averages the values obtained from Voigt and Reuss approximations, is defined as:

$$B_H = \frac{1}{2}(B_v + B_R) \quad (13)$$

$$G_H = \frac{1}{2}(G_v + G_R) \quad (14)$$

Young's modulus (E) and Poisson's ratio ($\upsilon$) are derived using the relations [57]:

$$E = \frac{9BG}{3B+G} \quad (15)$$

$$\upsilon = \frac{3B-2G}{2(3B+G)} \quad (16)$$

These moduli were calculated and are listed in Table 3. Also, the bulk, shear, and Young's modulus are presented in Fig. 2 as a function of Cr concentration. The bulk modulus is indicative of the cohesive or bonding energy of atoms in crystals and is often used as a measure of atomic bonding strength [60].

As shown in Fig. 2, the $Cr_xMo_{1-x}S_2$ bulk modulus fluctuates with increasing Cr concentration, directly reflecting the variation in atomic bond strength within the crystal structure. Notably, the average value of the bulk modulus (Hill approximation) increases slightly at different Cr concentrations (x = 0.125, 0.25, 0.75, and 0.875). This suggests a corresponding increase in atomic bond strength at these concentrations. The observed fluctuations indicate that the incorporation of Cr atoms affects the bonding environment, leading

**Table 3** Calculated bulk moduli (GPa) $B_V$, $B_R$, and $B_H = (B_V + B_R)/2$, shear moduli (GPa) $G_V$, $G_R$, and $G_H = (G_V + G_R)/2$, young moduli (GPa) $E_V$, $E_R$, and $E_H = (E_V + E_R)/2$, Poisson's ratio, $\nu_V$, $\nu_R$, and $\nu_H = (\nu_V + \nu_R)/2$, the universal elastic anisotropy index $A^U$, pugh rule B/G, microhardness H, and machinability index μ, for $Cr_xMo_{1-x}S_2$

| | $B_V$ | $B_R$ | $B_H$ | $G_V$ | $G_R$ | $G_H$ | $E_V$ | $E_R$ | $E_H$ | $\nu_R$ | $\nu_R$ | $\nu_H$ | $A^U$ | B/G | H | μ |
|---|---|---|---|---|---|---|---|---|---|---|---|---|---|---|---|---|
| $MoS_2$ | 56.6 | 10.8 | 33.7 | 38.9 | 7.3 | 23.1 | 95.0 | 17.9 | 56.5 | 0.22 | 0.22 | 0.22 | 25.7 | 1.45 | 4.3 | 9.1 |
| $Cr_{0.125}Mo_{0.875}S_2$ | 59.4 | 19.3 | 39.3 | 41.1 | 9.8 | 25.4 | 100.1 | 25.1 | 62.6 | 0.21 | 0.28 | 0.23 | 17.5 | 1.54 | 4.5 | 8.1 |
| $Cr_{0.250}Mo_{0.750}S_2$ | 59.6 | 16.7 | 38.2 | 40.7 | 8.6 | 24.6 | 99.4 | 22.1 | 60.8 | 0.22 | 0.28 | 0.25 | 21.0 | 1.55 | 4.0 | 9.0 |
| $Cr_{0.375}Mo_{0.625}S_2$ | 51.34 | 4.5 | 27.9 | 34.7 | 1.7 | 18.2 | 84.9 | 4.6 | 44.8 | 0.22 | 0.32 | 0.27 | 104.1 | 1.53 | 2.7 | 39.8 |
| $Cr_{0.500}Mo_{0.500}S_2$ | 50.98 | 5.3 | 28.1 | 34.1 | 2.6 | 18.3 | 83.6 | 6.8 | 45.2 | 0.22 | 0.28 | 0.25 | 68.0 | 1.53 | 3.0 | 21.6 |
| $Cr_{0.625}Mo_{0.375}S_2$ | 50.9 | 4.4 | 27.7 | 34.5 | 1.5 | 18.0 | 84.5 | 4.0 | 44.3 | 0.22 | 0.34 | 0.28 | 120.3 | 1.53 | 2.5 | 55.4 |
| $Cr_{0.750}Mo_{0.250}S_2$ | 60.0 | 11.2 | 35.6 | 41.9 | 6.2 | 24.1 | 102.1 | 15.7 | 58.9 | 0.21 | 0.26 | 0.24 | 33.0 | 1.47 | 4.1 | 11.5 |
| $Cr_{0.875}Mo_{0.125}S_2$ | 59.3 | 12.1 | 35.7 | 42.5 | 8.7 | 25.6 | 102.9 | 21.0 | 61.9 | 0.21 | 0.21 | 0.21 | 22.9 | 1.39 | 4.9 | 8.5 |
| $CrS_2$ | 40.1 | 16.1 | 28.1 | 25.3 | 12.7 | 19.0 | 62.7 | 30.2 | 46.4 | 0.24 | 0.18 | 0.21 | 6.4 | 1.47 | 3.7 | 3.6 |

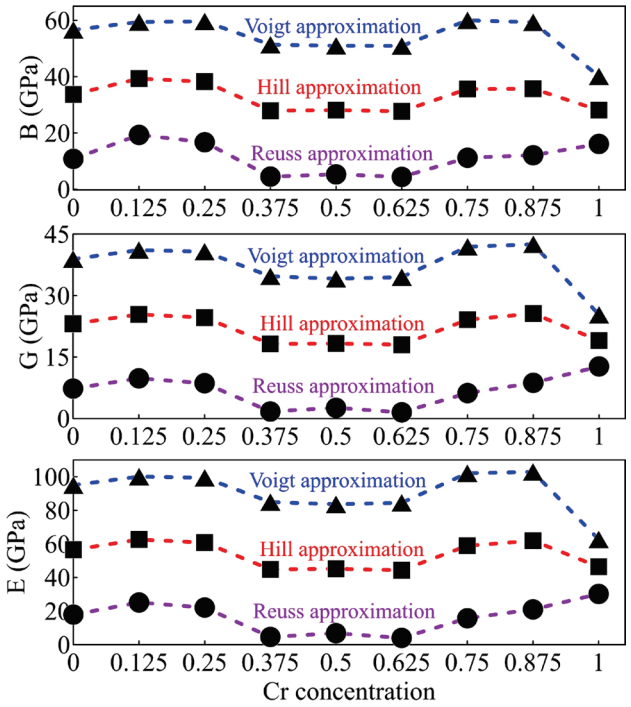


**Figure 2** Variation of bulk moduli (B), shear moduli (G), and Young's moduli (E) in $Cr_xMo_{1-x}S_2$ alloys as a function of Cr concentration. Purple dashed lines (Reuss approximation), red dashed lines (Hill approximation), and blue dashed lines (Voigt approximation) are included to aid visual interpretation.

to variations in the mechanical properties of the alloys. These changes are indicative of the complex interplay between Cr concentration and the structural stability of $Cr_xMo_{1-x}S_2$.

The shear modulus is a crucial parameter in assessing the elastic properties of materials, as it reflects their resistance to shear deformation and influences the motion of dislocations in a solid [61, 62]. A higher shear modulus indicates greater resistance to such deformation. In this study, as shown in Fig. 2, the behavior of the shear modulus using Voigt, Reuss, and Hill approximations with respect to Cr concentration (x) changes similarly to the behavior of the bulk modulus.

Additionally, Young's modulus, which measures the degree of stiffness in a crystal [63], also follows a similar trend using the Voigt, Reuss, and Hill approximations. This consistency suggests that by varying the concentration of Cr in $MoS_2$, we can tailor the material's resistance to shear deformation and its overall stiffness. Such tunability can potentially optimize the material for specific mechanical applications, enhancing its performance in fields that require specific elastic properties.

Poisson's ratio, which describes the ratio of transverse contraction to longitudinal strain when a material is stretched or compressed, typically ranges between -1 and 0.5 [64]. This ratio characterizes materials as non-auxetic (positive ratio) or auxetic (negative ratio) [65, 66]. In our study, the Poisson's ratio for all alloys falls between 0.2 and 0.3, classifying them as non-auxetic materials (Table 3).

The universal elastic anisotropy index $A^U$, which quantifies the directional dependence of elastic moduli in crystals, is calculated as $A^U = 5\frac{G_v}{G_R} + \frac{B_v}{B_R} - 6$ [59]. An anisotropy index of 1 indicates isotropic properties, while values different from 1 signify anisotropic behavior [67]. For all Cr concentrations in our study, $A^U$ exceeds 1, indicating elastic anisotropy in all compounds. Notably, $Cr_{0.375}Mo_{0.625}S_2$ and $Cr_{0.625}Mo_{0.375}S_2$ alloys exhibit the highest elastic anisotropy, implying a greater tendency for microcracking due to their elastic properties.

Furthermore, we calculated the microhardness parameter $H = \frac{(1-2\upsilon)E}{6(1+\upsilon)}$, indicating resistance to compression [68], the machinability index $\mu = \frac{B}{C_{44}}$, assessing ease of cutting [52], and the Pugh's ratio $\frac{B}{G}$, which determines material brittleness or ductility [69]. A Pugh's ratio greater than 1.75 suggests ductility, while a lower value indicates brittleness [70]. Our findings reveal that all studied alloys are brittle. However, the $Cr_{0.375}Mo_{0.625}S_2$ and $Cr_{0.625}Mo_{0.375}S_2$ alloys, with high elastic anisotropy and machinability index along with low microhardness, emerge as particularly suitable for mechanical applications, offering enhanced machinability compared to the other alloys.

## Electronic properties

To assess the electronic properties of $Cr_xMo_{1-x}S_2$ alloys, their band structures were calculated using the GGA approach, incorporating spin–orbit interaction. It is important to note that the GGA approach in DFT calculations often underestimates the energy bandgaps due to self-interaction errors. Therefore, the modified Becke–Johnson potential (mBJ-GGA) approach and hybrid functionals, known for providing more accurate energy bandgaps, were also employed [71, 72]. As indicated in Fig. 3, the minimum energy bandgaps (highlighted by the orange line) reveal that these

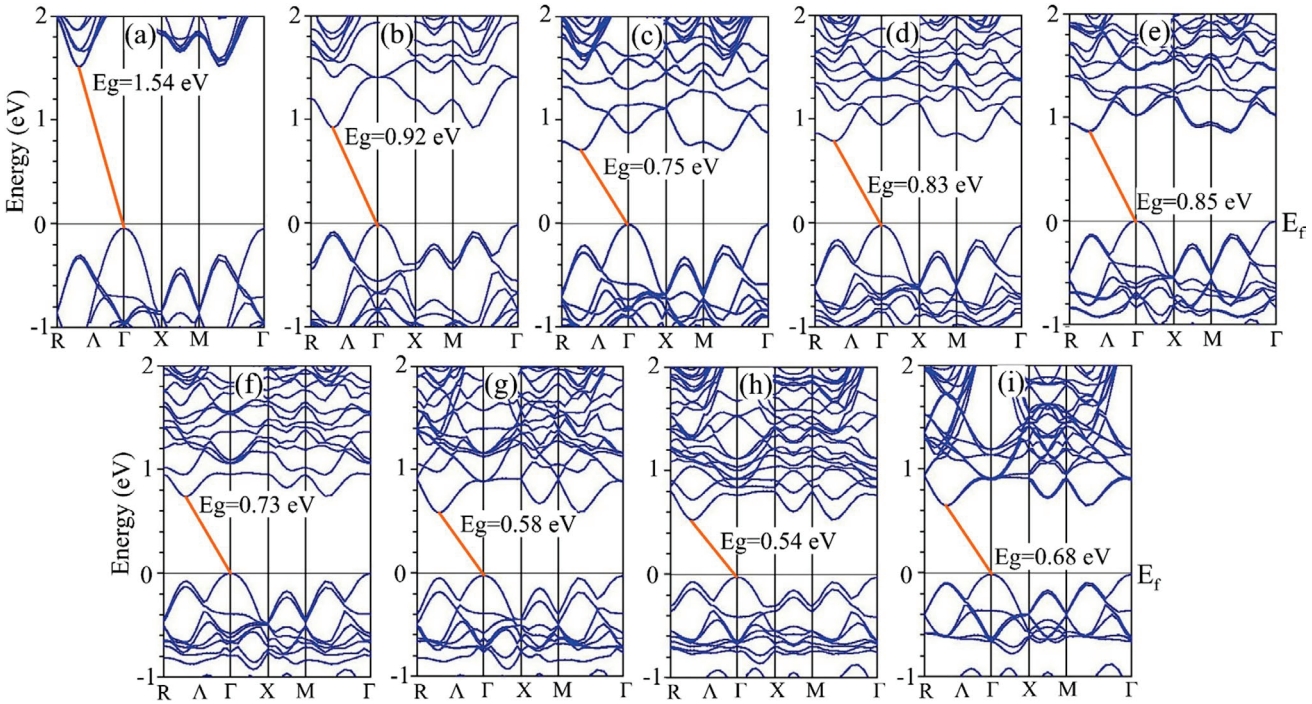


**Figure 3** Band structure of **a** $MoS_2$ **b** $Cr_{0.125}Mo_{0.875}S_2$ **c** $Cr_{0.250}Mo_{0.750}S_2$ **d** $Cr_{0.375}Mo_{0.625}S_2$ **e** $Cr_{0.500}Mo_{0.500}S_2$ **f** $Cr_{0.625}Mo_{0.375}S_2$ **g** $Cr_{0.750}Mo_{0.250}S_2$ **h** $Cr_{0.875}Mo_{0.125}S_2$ alloys and **i** $CrS_2$. Vertical lines indicate high-symmetry points in the first Brillouin zone. Orange lines show minimum energy bandgap and the horizontal lines at zero energy show the Fermi energy level.

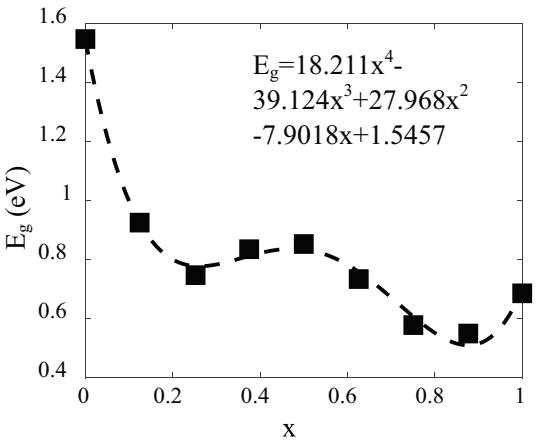


**Figure 4** Variation of minimum bandgaps ($E_g$) in $Cr_xMo_{1-x}S_2$ alloys as a function of chromium concentration (x), with the trend line represented by a dashed line indicating a fitted fourth-order polynomial function.

alloys are semiconductors with indirect energy bandgaps occurring between the Γ – Λ symmetry points. The energy bandgap varies from 1.54 eV in $MoS_2$ to 0.54 eV in $Cr_{0.875}Mo_{0.125}S_2$. Figure 4 presents these changes as a function of Cr concentration.

A notable trend is observed: with an increase in Cr concentration, the energy bandgap initially decreases up to $Cr_{0.250}Mo_{0.750}S_2$, then increases at $Cr_{0.375}Mo_{0.625}S_2$ and $Cr_{0.500}Mo_{0.500}S_2$, before decreasing again continuously up to $Cr_{0.875}Mo_{0.125}S_2$. This fluctuation can be attributed to two primary factors: crystalline volume/atomic size and Cr concentration. Experimentally, it has been shown that an increase in crystalline volume and a decrease in atomic size generally lead to an increase in energy bandgap due to elongated bond lengths and compressed atomic bands [73]. This observation is consistent with the data in Table 1, where $Cr_{0.375}Mo_{0.625}S_2$ and $Cr_{0.500}Mo_{0.500}S_2$ show a decrease in atomic size, contributing to an increased energy bandgap. Additionally, the bandgap narrowing effect, often observed at high atom concentrations, is attributed to the overlapping Cr concentration bands formed by overlapped Cr states [74]. This effect is believed to be responsible for the continuous decrease in the energy bandgap at higher Cr concentrations from $Cr_{0.625}Mo_{0.375}S_2$ to $Cr_{0.875}Mo_{0.125}S_2$ (Fig. 3 (f–h)). In the $CrS_2$ compound, an increase in both crystalline volume and Cr concentration leads to an increase in the bandgap (Fig. 3 (i)).

The comparison of energy bandgaps calculated with both GGA and mBJ-GGA approaches, as well as previously reported data, is summarized in Table 4. $Cr_{0.875}Mo_{0.125}S_2$ exhibits the lowest energy bandgap. The mBJ-GGA approach predictions are in good agreement with theoretical and experimental data from prior studies.

To elucidate the distribution of electrons near the Fermi energy, the DOS was analyzed. Figure 5 displays the DOS for Cr-doped $MoS_2$ structures at various concentrations. It is observed that for both $CrS_2$ and $MoS_2$ compounds, the valence band maximum (VBM) and conduction band minimum (CBM) are predominantly influenced by Cr_$d_{z^2}$ and Mo_$d_{z^2}$ orbitals, respectively. At all Cr concentrations (x = 0.125 to 0.875), Cr_$d_{z^2}$ orbitals play a major role in shaping the VBM and CBM. Additionally, $MoS_2$, $CrS_2$, and their alloys retain their semiconducting nature in the 2H phase. According to ligand field theory, this semiconducting behavior is attributed to the filled $d_{z^2}$ and empty $d_{xy}$ and $d_{x^2-y^2}$ orbitals [20]. Notably, the incorporation of Cr significantly reduces the energy bandgap, with a reduction from 1.54 to 0.92 eV even at a low Cr concentration (x = 0.125). This indicates that Cr doping has a profound impact on the energy bandgap and electronic properties of $MoS_2$. Furthermore, the presence of Cr atoms brings the Fermi energy level closer to the VBM, owing to the isoelectronic nature of Mo and Cr atoms, as well as the reduced atomic size and band count.

## Optical properties

The optical properties of $Cr_xMo_{1-x}S_2$ alloys can be analyzed through the dielectric function $\varepsilon(\omega)$, which characterizes the response of a crystal to electromagnetic waves. The dielectric function is expressed as a complex number:

$$\varepsilon(\omega) = \varepsilon_1(\omega) + i\varepsilon_2(\omega) \tag{17}$$

Here, $\varepsilon_1(\omega)$ and $\varepsilon_2(\omega)$ represent the real and imaginary parts of the dielectric function, respectively. The real and imaginary parts are interconnected by the Kramers–Kronig relation [75]:

$$\varepsilon_1(\omega) = 1 + \frac{2}{\pi} p \int_0^{\infty} \frac{\varepsilon_2(\omega')\omega' d\omega'}{\omega'^2 - \omega^2} \tag{18}$$

The dielectric function $\varepsilon(\omega)$ is influenced by transitions between discrete bands (interband transitions) and transitions within individual bands crossing the Fermi level (intraband transitions). Interband transitions are divided into direct and indirect transitions. Indirect transitions, often resulting from electron–phonon interactions, have a minor contribution to $\varepsilon(\omega)$ and are usually disregarded [76]. The significant part, the direct interband transitions, is obtained by calculating the imaginary part of the dielectric function $\varepsilon_2(\omega)$ and summing over all transitions from occupied valence states to unoccupied conduction band states:

$$\varepsilon_{2inter}(\omega) = \frac{Ve^2}{2\pi\hbar m^2\omega^2} \int d^3k \sum \left\{ |kn|p|kn'|^2 f(kn) \times \left(1 - f\left(kn'\right)\right)\delta\left(E_{kn} - E_{kn'} - \hbar\omega\right) \right\} \tag{19}$$

Here, ħω is the incident photon energy, $p$ is the momentum operator, $|kn\rangle$ denotes the eigenfunction with eigenvalue $E_{nk}$, and $f(kn)$ is the Fermi–Dirac distribution function [77].

**Table 4** Energy bandgaps of pristine $MoS_2$, $CrS_2$, and $MoS_2$ alloys with varying Cr concentrations: comparison of values obtained using GGA with SO, GGA without SO, and mBJ_GGA with SO, alongside experimental results

| Bandgap energy | GGA with SO (eV) | GGA without SO (eV) | mBJ_GGA With SO (eV) | Previous results | Ref |
|---|---|---|---|---|---|
| $MoS_2$ | 1.33 | 1.33 | 1.54 | 1.42 | [82] |
| | | | | Exp. 1.23 | [83] |
| $Cr_{0.125}Mo_{0.875}S_2$ | 0.82 | 0.83 | 0.92 | | |
| $Cr_{0.250}Mo_{0.750}S_2$ | 0.67 | 0.64 | 0.75 | | |
| $Cr_{0.375}Mo_{0.625}S_2$ | 0.75 | 0.73 | 0.83 | | |
| $Cr_{0.500}Mo_{0.500}S_2$ | 0.76 | 0.76 | 0.85 | | |
| $Cr_{0.625}Mo_{0.375}S_2$ | 0.65 | 0.65 | 0.73 | | |
| $Cr_{0.750}Mo_{0.250}S_2$ | 0.53 | 0.53 | 0.58 | | |
| $Cr_{0.875}Mo_{0.125}S_2$ | 0.46 | 0.46 | 0.54 | | |
| $CrS_2$ | 0.63 | 0.63 | 0.68 | 0.58, 0.60 | [82] |

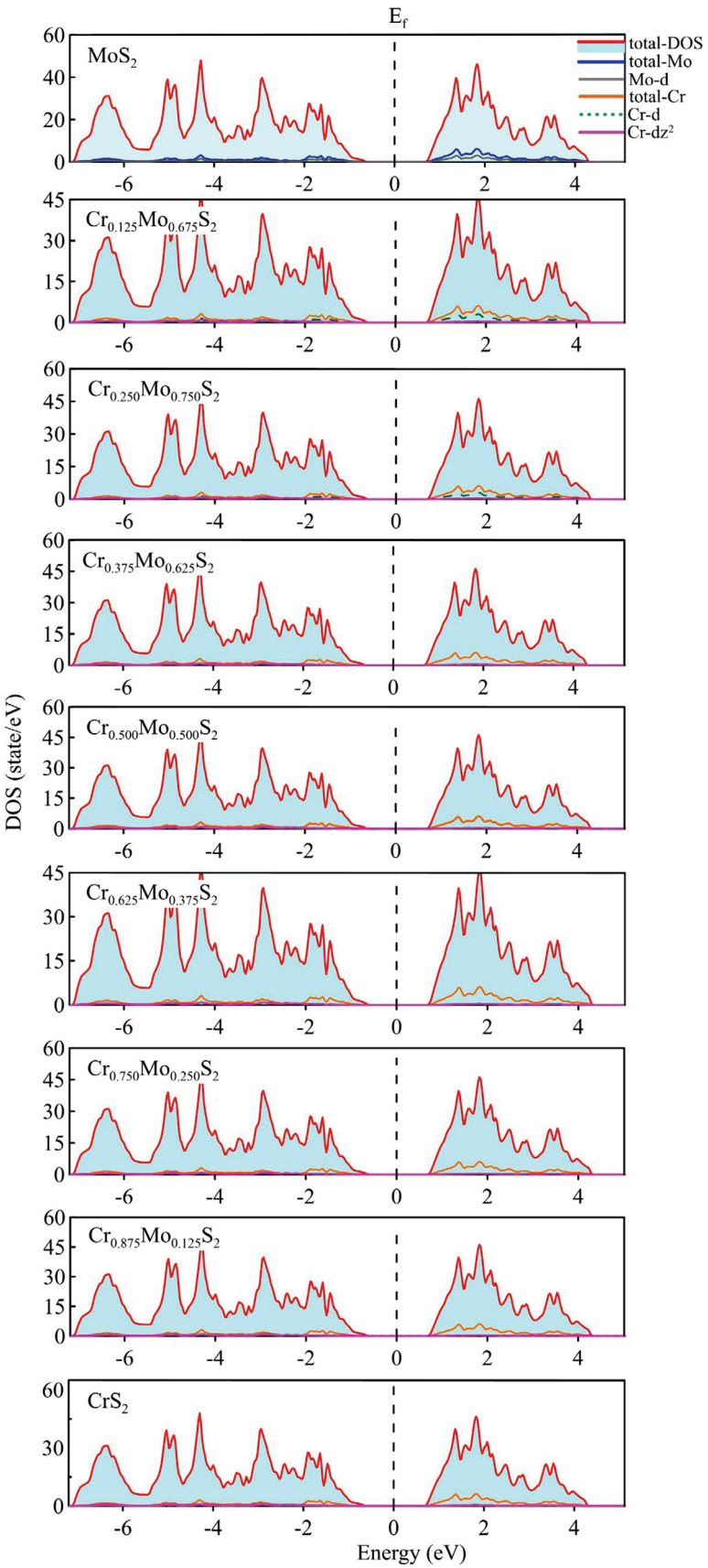


**Figure 5** Density of states (DOS) for pristine $MoS_2$, $CrS_2$, and $MoS_2$ alloys at varying Cr concentrations, illustrated with red lines and light blue shadows. The blue and gray lines represent the total (total-Mo) and d-orbitals (Mo-d) DOS of Mo atoms, respectively. The orange lines, green dashed lines, and purple lines depict the total (total-Cr), d-orbitals (Cr-d), and $z^2$ component of d-orbitals (Cr-$d_{z^2}$) in Cr atoms, respectively. Dashed vertical lines mark the Fermi level.

Other optical coefficients, such as absorption ($\alpha(\omega)$), reflectivity ($R(\omega)$), and refractive index ($n(\omega)$), are derived from the real and imaginary parts of the dielectric function [75]:

$$\alpha(\omega) = \frac{\sqrt{2}\omega}{c}\left(\sqrt{\varepsilon_1^2(\omega)+\varepsilon_2^2(\omega)} - \varepsilon_1(\omega)\right)^{1/2} \quad (20)$$

$$R(\omega) = \left|\frac{\sqrt{\varepsilon_1(\omega)+i\varepsilon_2(\omega)}-1}{\sqrt{\varepsilon_1(\omega)+i\varepsilon_2(\omega)}+1}\right|^2 \quad (21)$$

$$n(\omega) = \left(\frac{\sqrt{\varepsilon_1^2(\omega)+\varepsilon_2^2(\omega)}+\varepsilon_1(\omega)}{2}\right)^{1/2} \quad (22)$$

For the analysis of the optical characteristics of $Cr_xMo_{1-x}S_2$, the real and imaginary parts of the dielectric function, along with the optical coefficients, were calculated and analyzed for various Cr concentrations (x). The hexagonal structure of $Cr_xMo_{1-x}S_2$ imparts two independent components to the dielectric constant, $\varepsilon_X(\omega)$ and $\varepsilon_Z(\omega)$. This structural aspect leads to distinct optical properties in the X and Z directions of the crystal.

Figure 6 illustrates the real and imaginary parts of the dielectric function for different Cr concentrations (x = 0, 0.125, 0.250, 0.375, 0.500, 0.675, 0.75, 0.875, and 1) in the X and Z directions of $Cr_xMo_{1-x}S_2$. With increasing Cr concentration, the peaks of $\varepsilon_{1X}(\omega)$, $\varepsilon_{1Z}(\omega)$, $\varepsilon_{2X}(\omega)$ and $\varepsilon_{2Z}(\omega)$ shift toward lower energy values. Notably, a sharp increase at low energies in $\varepsilon_{2X}(\omega)$ is observed, attributed to the significant effect of the Drude term, especially at about 0.5 and 2 eV for X and Z directions, respectively. This variation is due to differences in plasma frequency, given by $\omega_p^2 = 4\pi e^2 n_e/m_e$.

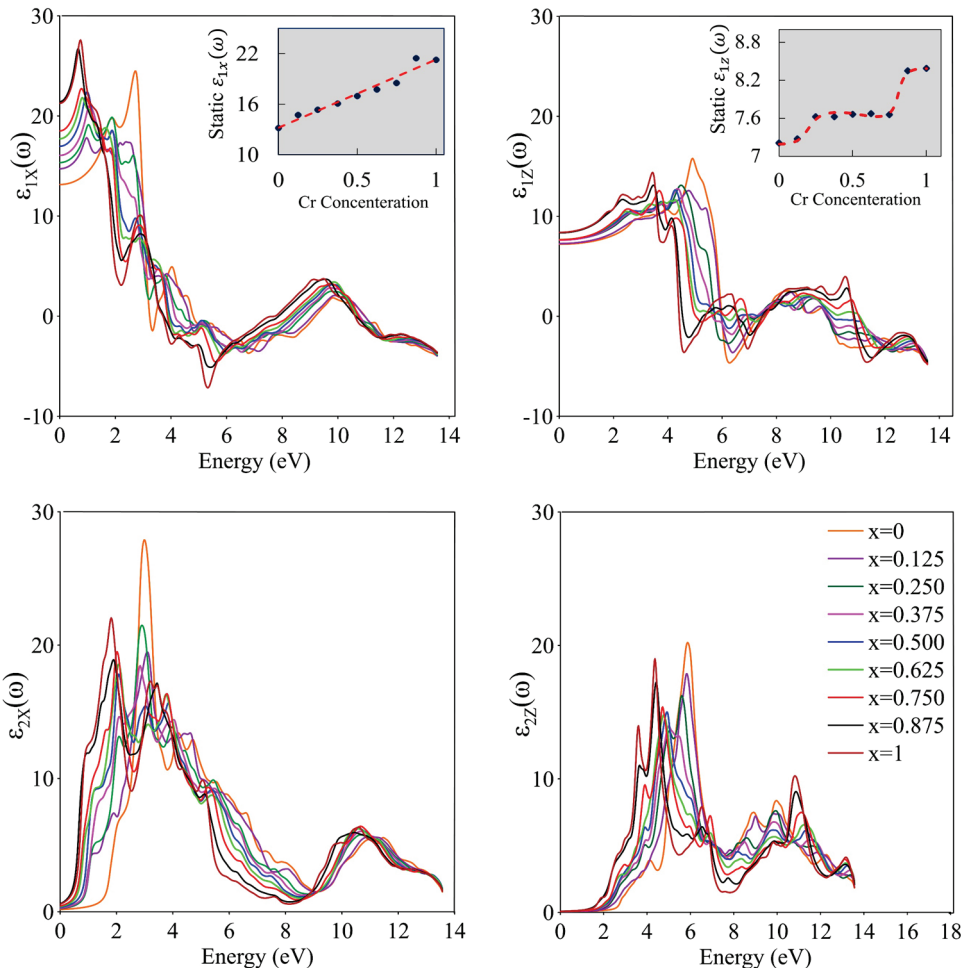


**Figure 6** Real ($(\varepsilon_{1_X}(\omega) and \varepsilon_{1_Z}(\omega)$) and imaginary ($(\varepsilon_{2_X}(\omega) and \varepsilon_{2_Z}(\omega)$)) parts of the dielectric function for $Cr_xMo_{1-x}S_2$ alloys across varying Cr concentrations (x). Insets with gray backgrounds depict the static real part of the dielectric function as a function of Cr concentration. Red dashed lines are included to aid visual interpretation.

For enhanced interpretability of the results, we applied fitting methods, focusing on the $R^2$ parameter as a measure of model accuracy [78, 79]. The static real part of the dielectric function at zero energy is illustrated in the $\varepsilon_{1X}(\omega)$ and $\varepsilon_{1Z}(\omega)$ plots of Fig. 6, highlighted with a gray background and fitted with linear and sixth-degree polynomial functions, respectively (red dashed lines). The static $\varepsilon_{1X}(\omega)$ shows a linear trend with the fitted function $\varepsilon_{1X}(0) = 8.0769x + 13.206$ and $R^2$ value of 0.959. In contrast, $\varepsilon_{1Z}(\omega)$ displays a step-like behavior, indicating a more complex behavior in the static $\varepsilon_{1Z}(\omega)$ compared to the $\varepsilon_{1X}(\omega)$.

Figure 7 presents the refractive index of $Cr_xMo_{1-x}S_2$ in both X and Z directions. The refractive index is crucial due to its direct relationship with microscopic interactions. With increasing Cr concentration, a redshift in the refractive index peak is observed in both directions. In the X direction, the maximum refractive peaks occur between 0.5 to 3.5 eV, spanning from infrared (IR) to ultraviolet (UV) spectrum ranges. Notably, two peaks in the blue light energy range are seen for $n_X(\omega)$ at x = 0.250 and 0.500 concentrations. In the Z direction, the refractive peaks appear in the UV range for all alloys. The static refractive index in both X and Z directions is also highlighted in Fig. 7 and fitted with polynomial functions (red dashed lines). The statistical $n_X(\omega)$ shows a linear behavior with the fitted function $n_X(0) = 0.9723x + 3.6544$ and $R^2$ of 0.966, while the statistical $n_Z(\omega)$ exhibits a more complex step-like behavior.

Figure 8 displays the reflectivity index, R(ω), for $Cr_xMo_{1-x}S_2$ alloys in both X and Z directions. Notably, within the visible light spectrum, $R_X(\omega)$ exceeds $R_Z(\omega)$. Peaks in $R_X(\omega)$ are observed in the 3 to 3.5 eV range for x = 0, 0.125, 0.250, 0.375, and in the 5.5 to 6.5 eV range for x = 0.500, 0.675, 0.75, 0.875, and 1. Conversely,

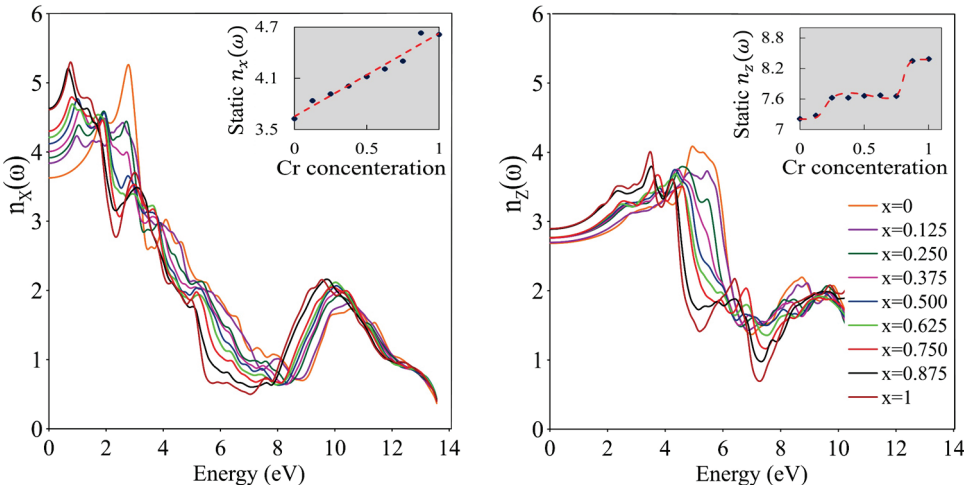


**Figure 7** Refractive index profiles of $Cr_xMo_{1-x}S_2$ alloys in X ($n_X(\omega)$) and Z ($n_Z(\omega)$) directions across different Cr concentrations (x). Insets on gray backgrounds depict the static refractive index as a function of Cr concentration. Red dashed lines are included to aid visual interpretation.

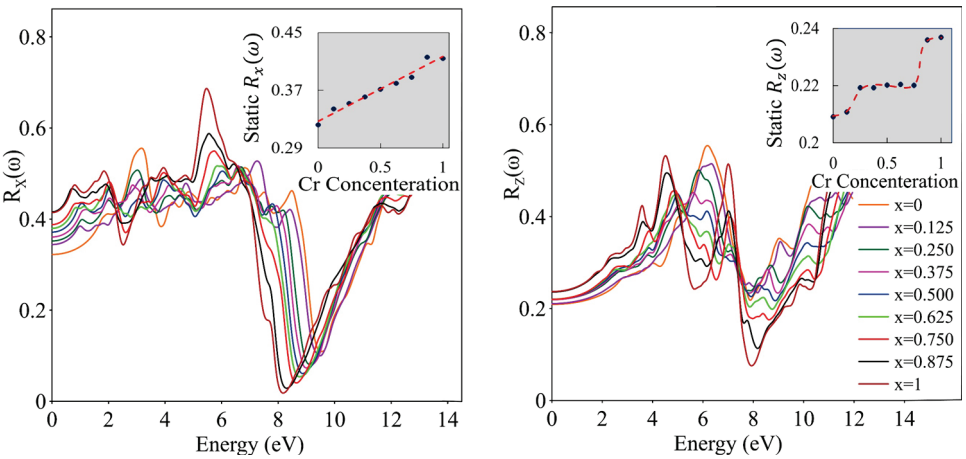


**Figure 8** Reflection coefficients of $Cr_xMo_{1-x}S_2$ alloys for varying chromium concentrations (x) in X ($R_X(\omega)$) and Z ($R_Z(\omega)$) directions. Insets with gray backgrounds illustrate the static reflection index as a function of Cr concentration. Red dashed lines are included to aid visual interpretation.

$R_Z(\omega)$ peaks in the 4.5 to 7.5 eV energy range, shifting toward lower energies with increasing x. Beyond 7.5 eV, a marked decline in the reflection spectrum is seen in both directions, attributed to collective plasmon resonance excitations.

The static reflectivity index of $Cr_xMo_{1-x}S_2$ alloys in the X and Z directions is also illustrated in Fig. 8, highlighted with a gray background and fitted using polynomial functions (red dashed lines). The static $R_X(\omega)$ demonstrates a linear trend with the fitted function $R_X(0) = 0.0899x + 0.3271$ and $R^2$ of 0.970. In contrast, the static $R_Z(0)$ exhibits a more complex step-like behavior.

The electron energy loss function $L(\omega)$) for $Cr_xMo_{1-x}S_2$ is calculated and shown in Fig. 9. The peaks in L(ω), representing the plasmon frequency, occur at energies where the real part of the dielectric function, $\varepsilon_1(\omega)$, approaches zero. The plasmon frequency and its magnitude are related to the collective oscillation and the density of valence electrons, respectively. Considering that the CrxMo1-xS2 energy loss spectrum does not show significant values at energies smaller than 21.5 eV, it can be concluded that the energy of incident photons causes excitation and electron transitions between energy levels.

In the high-energy range of 21.5–23 eV, there is a single sharp peak for each Cr concentration in both the X and Z directions. For x = 0, 0.125, 0.25, 0.375, 0.50, 0.625, 0.75, 0.875, and 1, the peaks occur at 22.98, 22.70, 22.54, 22.43, 22.35, 22.13, 22.02, 21.89, and 21.83 eV in the X direction, and 22.68, 22.65, 22.46, 22.40, 22.29, 22.24, 22.16, 22.05, and 22.04 eV in the Z direction, respectively. The value of L(ω) in the Z direction is generally higher than the corresponding value in the X direction.

As highlighted with a gray background in Fig. 9 and fitted using polynomial functions, the $L_X(\omega)$ peak is described by − 1.116x + 22.877–1.116x + 22.877 − 1.116x + 22.877 with an $R^2$ of 0.979, and the $L_Z(\omega)$ peak is described by − 0.6827x + 22.671–0.6827x + 22.671 − 0.6827x + 22.671 with an $R^2$ of 0.975 (red dashed lines). With increasing Cr concentration, these peaks decrease and shift toward lower energies. This behavior can be explained by the differences in the density of valence electrons, which cause variations in L(ω) peaks in different directions and concentrations. Furthermore, at frequencies higher than the plasmon frequency, $Cr_xMo_{1-x}S_2$ alloys can suddenly transmit light, leading to a decrease in reflectivity (Fig. S2).

The absorption spectrum, encompassing both interband and intraband transitions, is illustrated in Fig. 10 for $Cr_xMo_{1-x}S_2$ alloys along X and Z directions. The interband absorption arises from electron-photon interactions, prompting electronic transitions between occupied valence states and unoccupied conduction states near the Fermi energy. Multiple interband and intraband absorption peaks in $\alpha_X(\omega)$ and $\alpha_Z(\omega)$ are observed within the 0 to 14 eV energy range. Particularly, from 5 to 8 eV, a distinct peak is noticeable in both $\alpha_X(\omega)$ and $\alpha_Z(\omega)$. In the visible light spectrum, $\alpha_X(\omega)$ exhibits peaks corresponding to yellow and blue light energies, specifically for X = 0.500, 0.675, 0.75, 0.875, 1, and X = 0, 0.125, 0.250, 0.375, respectively.

## Conclusion

This study extensively investigated the structural, mechanical, electronic, and optical properties of $MoS_2$ alloyed with chromium (Cr) atoms. Structurally, the

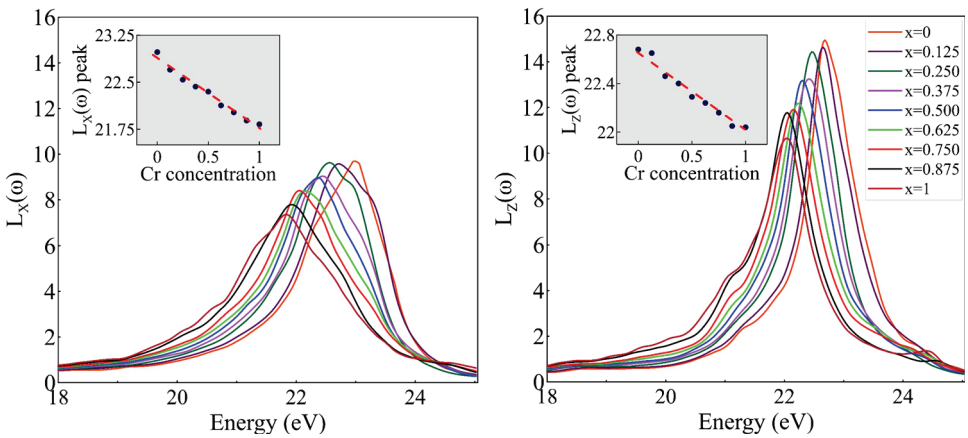


**Figure 9** The electron energy loss function for $CrxMo_{1-x}S_2$ alloys across varying Cr concentrations (x), shown in X direction ($L_X(\omega)$) and Z direction ($L_Z(\omega)$). Insets with gray backgrounds illustrate the electron energy loss function as a function of Cr concentration. Red dashed lines are included to aid visual interpretation.

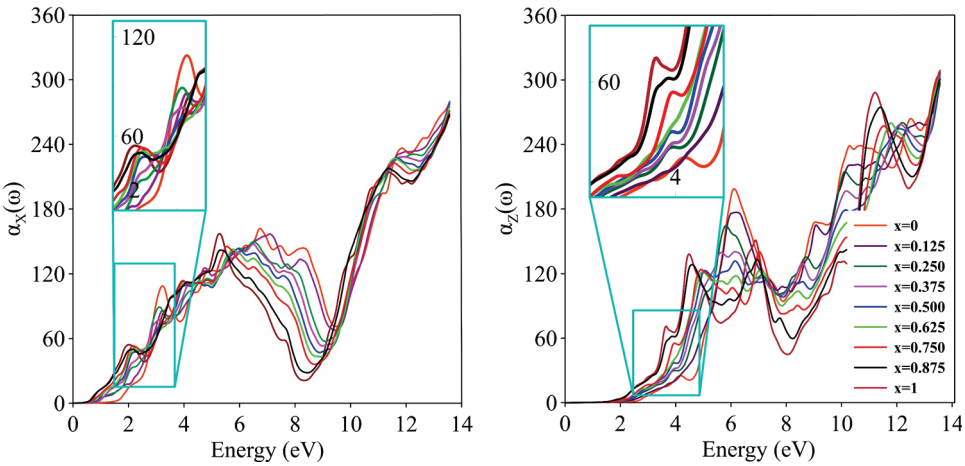


**Figure 10** Absorption coefficients for $CrxMo_{1-x}S_2$ alloys across varying Cr concentrations (x), shown in X direction ($\alpha_X(\omega)$) and Z direction ($\alpha_Z(\omega)$).

$Cr_xMo_{1-x}S_2$ alloys with both hexagonal ($MoS_2$, $CrS_2$, and $Cr_{0.500}Mo_{0.500}S_2$) and monoclinic phases were found to be thermodynamically stable across all Cr concentrations. Mechanically, all compounds were confirmed to be stable as per Born's inequalities. Notably, lower Cr concentrations (specifically $Cr_{0.125}Mo_{0.875}S_2$) enhanced atomic bond strength and elastic stiffness. Despite all alloys being anisotropic and brittle, $Cr_{0.375}Mo_{0.625}S_2$ and $Cr_{0.625}Mo_{0.375}S_2$ demonstrated high elastic anisotropy and machinability, along with low microhardness, making them more machinable compared to others.

Electronically, band structure and density of states (DOS) analyses using GGA and mBJ-GGA approaches revealed a decrease in bandgap with increasing Cr concentration, fluctuating from 1.54 eV in pure $MoS_2$ to 0.54 eV in $Cr_{0.875}Mo_{0.125}S_2$. The addition of Cr atoms significantly influenced the bandgap and DOS near the Fermi energy, with even a single Cr atom reducing the bandgap from 1.54 eV in $MoS_2$ to 0.92 eV in $Cr_{0.125}Mo_{0.875}S_2$. Unlike $MoS_2$, where Mo_ $d_{z^2}$ orbitals dominate near the Fermi energy, Cr_ $d_{z^2}$ orbitals play a significant role in the VBM and CBM of $Cr_xMo_{1-x}S_2$ alloys.

Optically, due to the hexagonal and monoclinic structures, the dielectric function of these alloys exhibited two independent components, $\varepsilon_X(\omega)$ and $\varepsilon_Z(\omega)$. Our findings showed that increasing Cr concentration led to a shift of maximum $\varepsilon(\omega)$, $\alpha(\omega)$, $n(\omega)$ and $R_Z(\omega)$ to lower energies. In the visible light spectrum, several peaks were observed in refractive ($n_X(\omega)$) and absorption ($\alpha_X(\omega)$) spectra, with specific peaks correlating to certain Cr concentrations.

These findings on the bandgap and optical properties suggest that $Cr_xMo_{1-x}S_2$ alloys are promising candidates for electronic and optical applications involving bandgap engineering. The unique combination of electronic, optical, and mechanical properties of these alloys holds potential for practical applications, contributing valuable insights to the field of material science.

## Acknowledgements

DV acknowledges funding support from the National Science Foundation (NSF) under grant number CBET-2110603.

## Author contributions

Behdad Moslehi performed investigation, methodology, software, data curation, formal analysis, and writing—original draft preparation; Zahra Nourbakhsh presented supervision, conceptualization, validation, formal analysis, resources, and writing—reviewing and editing. Daryoosh Vashaee analyzed supervision, validation, formal analysis, funding acquisition, and writing—reviewing and editing.

## Data availability

The datasets generated and analyzed during the current study are not publicly available due to their extensive size and complexity. However, they

are available from the corresponding author upon reasonable request and with sufficient notice.

## Declarations

**Conflicts of interest** The authors declare that they have no conflicts of interest.

**Supplementary Information** The online version contains supplementary material available at https://doi.org/10.1007/s10853-024-10197-3.

## References


[1] Jellison G Jr (1992) Optical functions of GaAs, GaP, and Ge determined by two-channel polarization modulation ellipsometry. Opt Mater 1(3):151–160

[2] Ameri M et al (2011) Structural and electronic properties calculations of $Al_x$ $In_{1-x}$ P Alloy. Mater Sci Appl 2(07):729

[3] Kumar S et al (2016) Band gap engineering of $CuAl_{1-x}In_xS_2$ alloys for photovoltaic applications: a first principles study. J Phys D Appl Phys 49(20):205103

[4] Adachi S (2009) Properties of semiconductor alloys: group-IV, III-V and II-VI semiconductors. Wiley, Hoboken

[5] Xie L (2015) Two-dimensional transition metal dichalcogenide alloys: preparation, characterization and applications. Nanoscale 7(44):18392–18401

[6] Liang L et al (2014) Electronic bandgap and edge reconstruction in phosphorene materials. Nano Lett 14(11):6400–6406

[7] Neto AC et al (2009) The electronic properties of graphene. Rev Mod Phys 81(1):109

[8] Zhang H (2015) Ultrathin two-dimensional nanomaterials. ACS Nano 9(10):9451–9469

[9] Hong Y-L et al (2020) Chemical vapor deposition of layered two-dimensional $MoSi_2N_4$ materials. Science 369(6504):670–674

[10] Zhang H, Li X-B, Liu L-M (2013) Tunable electronic and magnetic properties of $WS_2$ nanoribbons. J Appl Phys 114(9):093710

[11] Chhowalla M et al (2013) The chemistry of two-dimensional layered transition metal dichalcogenide nanosheets. Nat Chem 5(4):263–275

[12] Zhang H, Liu L-M, Lau W-M (2013) Dimension-dependent phase transition and magnetic properties of $VS_2$. J Mater Chem A 1(36):10821–10828

[13] Gutiérrez HR et al (2013) Extraordinary room-temperature photoluminescence in triangular $WS_2$ monolayers. Nano Lett 13(8):3447–3454

[14] Yuan X et al (2017) Structural stability and intriguing electronic properties of two-dimensional transition metal dichalcogenide alloys. Phys Chem Chem Phys 19(21):13846–13854

[15] Jing Y et al (2013) Metallic $VS_2$ monolayer: a promising 2D anode material for lithium ion batteries. J Phys Chem C 117(48):25409–25413

[16] Hwang H, Kim H, Cho J (2011) MoS2 nanoplates consisting of disordered graphene-like layers for high rate lithium battery anode materials. Nano Lett 11(11):4826–4830

[17] Zhuang HL et al (2014) Computational prediction and characterization of single-layer CrS2. Appl Phys Lett 104(2):022116

[18] Yu N et al (2015) Molybdenum disulfide as a highly efficient adsorbent for non-polar gases. Phys Chem Chem Phys 17(17):11700–11704

[19] Huang X et al (2017) Activating basal planes and S-terminated edges of $MoS_2$ toward more efficient hydrogen evolution. Adv Func Mater 27(6):1604943

[20] Habib MR et al (2019) Electronic properties of polymorphic two-dimensional layered chromium disulphide. Nanoscale 11(42):20123–20132

[21] Zhuang HL, Hennig RG (2013) Computational search for single-layer transition-metal dichalcogenide photocatalysts. J Phys Chem C 117(40):20440–20445

[22] Karunadasa HI et al (2012) A molecular $MoS_2$ edge site mimic for catalytic hydrogen generation. Science 335(6069):698–702

[23] Xiong Z et al (2021) Field-free improvement of oxygen evolution reaction in magnetic two-dimensional heterostructures. Nano Lett 21(24):10486–10493

[24] Zeng Z et al (2014) Growth of noble metal nanoparticles on single-layer $TiS_2$ and $TaS_2$ nanosheets for hydrogen evolution reaction. Energy Environ Sci 7(2):797–803

[25] Tian H et al (2016) Optoelectronic devices based on two-dimensional transition metal dichalcogenides. Nano Res 9:1543–1560

[26] Gong X et al (2022) Alternating magnetic field induced magnetic heating in ferromagnetic cobalt single-atom catalysts for efficient oxygen evolution reaction. Nano Lett 22(23):9411–9417

[27] Jiang Z et al (2023) Interlayer-confined NiFe dual atoms within $MoS_2$ electrocatalyst for ultra-efficient acidic overall water splitting. Adv Mater 35(32):2300505

[28] Berger M (2016) Nanotechnology: the future is Tiny. Royal society of chemistry, London

[29] Li X, Zhu H (2015) Two-dimensional $MoS_2$: properties, preparation, and applications. J Materiomics 1:33–44
[30] Chou SS et al (2013) Ligand conjugation of chemically exfoliated MoS2. J Am Chem Soc 135(12):4584–4587
[31] Shi H et al (2013) Strong ferromagnetism in hydrogenated monolayer $MoS_2$ tuned by strain. Phys Rev B 88(20):205305
[32] Conley HJ et al (2013) Bandgap engineering of strained monolayer and bilayer $MoS_2$. Nano Lett 13(8):3626–3630
[33] Su M et al (2022) Micro eddy current facilitated by screwed MoS2 structure for enhanced hydrogen evolution reaction. Adv Func Mater 32(22):2111067
[34] Gao Y et al (2013) Toward single-layer uniform hexagonal boron nitride–graphene patchworks with zigzag linking edges. Nano Lett 13(7):3439–3443
[35] Ci L et al (2010) Atomic layers of hybridized boron nitride and graphene domains. Nat Mater 9(5):430–435
[36] Yuge K (2009) Phase stability of boron carbon nitride in a heterographene structure: a first-principles study. Phys Rev B 79(14):144109
[37] Engel E (2011) Density functional theory. Springer, Berlin
[38] Tran, F., *WIEN2k: An Augmented Plane Wave Plus Local Orbitals Program for Calculating Crystal Properties*. 2018.
[39] Perdew JP, Burke K, Ernzerhof M (1996) Generalized gradient approximation made simple. Phys Rev Lett 77(18):3865
[40] Tran F, Blaha P (2017) Importance of the kinetic energy density for band gap calculations in solids with density functional theory. J Phys Chem A 121(17):3318–3325
[41] Fan X-L et al (2014) Site-specific catalytic activity in exfoliated MoS 2 single-layer polytypes for hydrogen evolution: basal plane and edges. J Mater Chem A 2(48):20545–20551
[42] Ataca C, Sahin H, Ciraci S (2012) Stable, single-layer $MX_2$ transition-metal oxides and dichalcogenides in a honeycomb-like structure. J Phys Chem C 116(16):8983–8999
[43] Chen K et al (2021) Diverse electronic and magnetic properties of $CrS_2$ enabling strain-controlled 2D lateral heterostructure spintronic devices. npj Comput Mater 7(1):79
[44] Feng L-Y et al (2020) Magnetic and topological properties in hydrogenated transition metal dichalcogenide monolayers. Chin J Phys 66:15–23
[45] Qi W, Wang M (2002) Size effect on the cohesive energy of nanoparticle. J Mater Sci Lett 21:1743–1745. https://doi.org/10.1023/A:1020904317133
[46] Yalameha S, Vaez A (2019) Structural, electronic, elastic and thermodynamic properties of $Al_{1-x}Z_xNi$ (Z= Cr, V and x= 0, 0.125, 0.25) alloys: first-principle calculations. Comput Condens Matter 21:e00415
[47] Song TT et al (2016) The stability of aluminium oxide monolayer and its interface with two-dimensional materials. Sci Rep 6(1):29221
[48] Pan H et al (2017) $C_4N_3H$ monolayer: a two-dimensional organic dirac material with high fermi velocity. Phys Rev B 96(19):195412
[49] Yalameha S et al (2021) Highly stable full Heusler order Cs (Na, K) 2Bi with diverse topological phases controlled by strain engineering. Mater Sci Eng, B 273:115430
[50] Yalameha S, Nourbakhsh Z, Vashaee D (2022) ElATools: A tool for analyzing anisotropic elastic properties of the 2D and 3D materials. Comput Phys Commun 271:108195
[51] Wang Z et al (2023) Energy transfer and patterning characteristics in pulsed-laser subtractive manufacturing of single layer of $MoS_2$. Int J Heat Mass Transf 204:123873
[52] Yamusa SA et al (2023) First-principles study on the structural, electronic, and elastic properties of transition metal dichalcogenides. Phys Access 3:133
[53] Peelaers H, Van de Walle C (2014) Elastic constants and pressure-induced effects in $MoS_2$. J Phys Chem C 118(22):12073–12076
[54] Wei L et al (2010) Electronic and elastic properties of $MoS_2$. Phys B 405(10):2498–2502
[55] Chen S-B et al (2020) Strain-induced electronic structures, mechanical anisotropy, and piezoelectricity of transition-metal dichalcogenide monolayer $CrS_2$. J Appl Phys 128(12):125111
[56] Hill R (1952) The elastic behaviour of a crystalline aggregate. Proc Phys Soc Sect A 65(5):349
[57] Schreiber E et al (1975) Elastic constants and their measurement. J Appl Mech 42(3):747–748
[58] Sun Z et al (2004) Calculated elastic properties of $M_2AlC$ (M= Ti, V, Cr, Nb and Ta). Solid State Commun 129(9):589–592
[59] Polich NG et al (2023) Cover crops effects on anisotropy of unsaturated soil hydraulic properties. Soil Tillage Res 227:105601
[60] Gschneidner KA Jr (1964) Physical properties and interrelationships of metallic and semimetallic elements. Solid state physics. Elsevier, pp 275–426
[61] Černý M, Pokluda J (2010) The theoretical shear strength of fcc crystals under superimposed triaxial stress. Acta Mater 58(8):3117–3123
[62] Saeidi P, Yalameha S (2019) The structural and elastic properties of $InSb_{1-x}Bi_x$ alloys. Comput Condens Matter 18:e00358
[63] Fast L et al (1995) Elastic constants of hexagonal transition metals: theory. Phys Rev B 51(24):17431
[64] Ross CT, Chilver A (1999) Strength of materials and structures. Elsevier, Amsterdam

[65] Ting, T. and D. Barnett, *Negative Poisson's ratios in anisotropic linear elastic media.* 2005.
[66] Yalameha S et al (2021) Promising bialkali bismuthides Cs(Na, K)$_2$Bi for high-performance nanoscale electromechanical devices: prediction of mechanical and anisotropic elastic properties under hydrostatic tension and compression and tunable auxetic properties. Nanomaterials 11(10):2739
[67] Ranganathan SI, Ostoja-Starzewski M (2008) Universal elastic anisotropy index. Phys Rev Lett 101(5):055504
[68] El-Adawy A, El-KheshKhany N (2006) Effect of rare earth ($Pr_2O_3$, $Nd_2O_3$, $Sm_2O_3$, $Eu_2O_3$, $Gd_2O_3$ and $Er_2O_3$) on the acoustic properties of glass belonging to bismuth–borate system. Solid State Commun 139(3):108–113
[69] Nassah Y et al (2023) Electronic band structure, mechanical and optical characteristics of new lead-free halide perovskites for solar cell applications based on DFT computation. Bull Mater Sci 46(2):55
[70] Yalameha S (2023) Effect of hydrostatic strain on the mechanical properties and topological phase transition of bi-alkali pnictogen $NaLi_2Bi$. Phys Scr 98(4):045905
[71] Ramzan M, Ahuja R (2011) Role of correlation effects in the superconducting material: $InV_6S_8$. Appl Phys Lett 99(22):221904
[72] Camargo-Martínez J, Baquero R (2013) The band gap problem: the accuracy of the Wien2k code confronted. Revista mexicana de física 59(5):453–459
[73] Para TA et al (2016) Grain size disposed structural, optical and polarization tuning in ZnO. Appl Phys A 122:1–9
[74] Auvergne D, Camassel J, Mathieu H (1975) Band-gap shrinkage of semiconductors. Phys Rev B 11(6):2251
[75] Wooten F (1972) Optical properties of solids. Princeton, Citeseer
[76] Smith NV (1971) Photoelectron energy spectra and the band structures of the noble metals. Phys Rev B 3(6):1862
[77] Ambrosch-Draxl C, Sofo JO (2006) Linear optical properties of solids within the full-potential linearized augmented planewave method. Comput Phys Commun 175(1):1–14
[78] Glantz SA, Slinker BK, Neilands T (1990) Primer of Applied Regression and Analysis of Variance''. Mc Graw Hill Inc, New York
[79] Draper NR, Smith H (1998) Applied regression analysis, vol 326. Wiley, Hoboken
[80] Pan Y, Guan W (2016) Effect of sulfur concentration on structural, elastic and electronic properties of molybdenum sulfides from first principles. Int J Hydrog Energy 41(26):11033–11041
[81] Schönfeld B, Huang J, Moss S (1983) Anisotropic mean-square displacements (MSD) in single-crystals of 2H-and 3R-$MoS_2$. Acta Crystallogr B 39(4):404–407
[82] Bastos CM et al (2019) Ab initio investigation of structural stability and exfoliation energies in transition metal dichalcogenides based on Ti-, V-, and Mo-group elements. Phys Rev Mater 3(4):044002
[83] Hulliger F (2012) Structural chemistry of layer-type phases, vol 5. Springer, Berlin